Spectral Graph Theory for Characterization and Homogenization of Grain Boundary Networks

Johnson, O.K., Lund, J.M., Critchfield, T.R.

Oliver Johnson
ojohnson@byu.edu

Original Publication Citation

Spectral Graph Theory for Characterization and Homogenization of Grain Boundary Networks, Johnson, O.K., Lund, J.M., Critchfield, T.R., *Acta Materialia*. vol. 146, March, pp. 42-54 (2018). doi: 10.1016/j.actamat.2017.11.054

Spectral Graph Theory for Characterization and Homogenization of Grain Boundary Networks

Oliver K. Johnson*, Jarrod M. Lund, Tyler R. Critchfield
Department of Mechanical Engineering, Brigham Young University, Provo, UT 84602
*email: ojohnson@byu.edu

October 20, 2017

Abstract

Grain boundary networks (GBNs) have a profound influence on the properties of both structural and functional materials. However, existing methods to characterize their complex structure have almost universally relied upon a binary classification of GBs as either "special" or "general", which ignores the rich and continuous spectrum of GB types and properties. Furthermore, characterizing the aggregate network structure of GBs has proven complicated, with traditional methods focusing on local structure and also relying on a binary GB taxonomy, e.g. by evaluating how many "special" or "general" boundaries meet at triple junctions or quadruple nodes. Here we develop new structural metrics for GBNs, based on spectral graph theory, that encode both global network topology and the full spectrum of constituent GB properties, enabling high-fidelity characterization of arbitrary GBNs. Using these metrics, we derive an new structure-property relation for GBN diffusivity. The dominant term in this expression provides an efficient and accurate approximation, whose corresponding spectral metrics reveal the dominant microstructural features influencing the property of interest. The spectral index of this term serves as a type of global order parameter that reveals a fundamental structural transition in GBNs. This work provides a new framework to characterize the structure of GBNs in greater generality than previously possible and facilitates the development of new defect-sensitive structure-property models.

Keywords: Grain Boundary, Networks, Homogenization, Diffusion, Spectral Graph Theory

1 Introduction

Grain boundaries (GBs) in polycrystalline materials form a complex network of inter-crystalline interfaces, whose collective structure strongly influences many materials phenomena including strength [1, 2], corrosion [1, 3, 4], stress-corrosion cracking [5], spallation [6], creep [7], hydrogen embrittlement [2], solar cell efficiency [8, 9], superconductivity [10], and nuclear fuel performance [11–13]. Because of the complexity of their combined crystallographic and topological degrees of freedom, grain boundary networks (GBNs) have historically been characterized using reduced order metrics. Computational and experimental studies (including our own) both routinely employ a binary classification of the constituent grain boundaries as either "special" or "general" and assign all boundaries of a given type identical properties (a few notable exceptions include [14–16]). It is also common to model grain boundary networks using simple idealized geometries as illustrated in Fig. 1a. In contrast, real grain boundary networks (Fig. 1b) are composed of a continuous spectrum of grain boundary types, whose properties span many orders of magnitude and whose topology is far more complex than what is captured by such idealizations. If

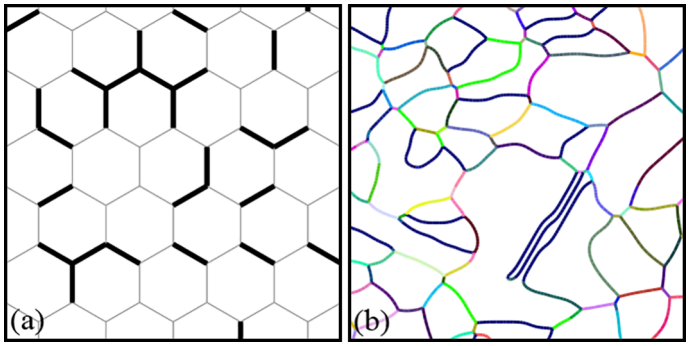

Figure 1: (a) Idealized model of a grain boundary network with general (high-angle) boundaries in light grey and special (low-angle) boundaries in bold black lines. (b) A real grain boundary network from a sample of Inconel 690 (data courtesy C.A. Schuh) with boundaries colored according to their misorientation [17].

the structure of grain boundary networks were better understood, it would be possible to devise novel processing routes to control it and, thereby, achieve substantial performance enhancements across all classes of polycrystalline materials.

A complete description of the structure of grain boundary networks requires specification of the character (e.g. crystallography or properties) of individual grain boundaries and how they are assembled. The network structure of grain boundaries may, at first, appear random, but is, in fact, highly correlated due to crystallographic constraints, processing history, and both kinetic and thermodynamic influences. Several approaches have been devised to quantitatively characterize various aspects of GBN structure; these include tools from percolation theory (e.g. correlation lengths, cluster sizes, etc.) [18], Betti numbers [19, 20], triple junction fractions [21–25], quadruple node fractions [26], swatches [27], and twin-related domain (TRD) sizes [28, 29]. These descriptions focus primarily on topological structure. Those that incorporate information about GB types employ the binary "special vs. general" taxonomy of boundaries. Building on this previous work, we develop a new technique to simultaneously characterize the complex topological structure of GBNs and the full spectrum of GB types/properties in arbitrary polycrystalline materials.

2 A New Approach

In the diverse fields of computer science, ecology, and biology, complex networks exist (e.g. plant-pollinator networks, or protein interaction networks) and have been analyzed using the mathematical tools of spectral graph theory (SGT) [30–34]. Perhaps the best known example is the PageRank algorithm that forms the core of Google's search engine [30, 34, 35]. PageRank models the complex network of internet websites as a graph (corresponding to a Markov Chain), which is represented as a matrix (the transition matrix). The PageRank—an importance metric used to determine the relevance of a website to a search query—is given by the principal eigenvector of this matrix. In other words, PageRank uses spectral decomposition of the network structure of the Web to determine its dominant features and correlate these with query relevance. By analogy, we hypothesize that spectral decomposition can be applied to the network structure of materials to characterize their dominant microstructural features and correlate these with material properties.

Studying an analogous problem for membranes, Marc Kac famously asked the question "Can one hear the shape of a drum?" [36], which was the title of a study in which the author investigated what information about the shape of a drum (or tambourine) could be inferred from its timbral spectrum. Here we ask a related question for grain boundary networks: "What can we learn about the complex

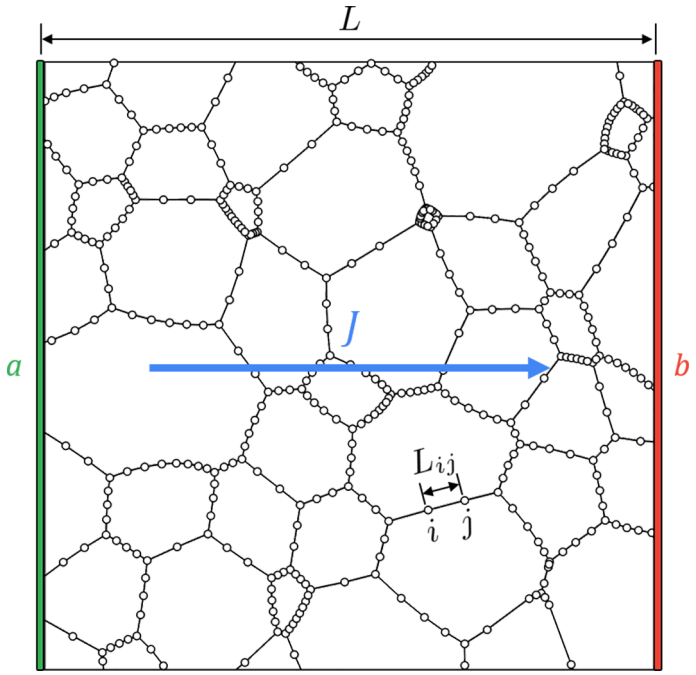

Figure 2: Discretization of a GBN showing nodes and edges. The source and sink supernodes are shown in green and red, respectively. The direction of the macroscopic flux, J, is indicated along with the sample length, L. Representative nodes, i and j are labeled along with the length of the edge connecting them, L_{ij}.

structure of grain boundary networks and their effective properties by analyzing their eigenvalues and eigenvectors?"

3 Methods

3.1 Eigendecomposition of a GBN and its Properties

We will consider two-dimensional GBNs, though the methods presented should be applicable to fully three-dimensional GBNs as well. A GBN is represented as an undirected weighted graph, defined by the ordered triplet $G = (V, E, W)$, via discretization, where V is the set of vertices (also called nodes), E is the set of edges, and W is the set of edge weights. Nodes (vertices) are located at triple junctions (TJs) and along GBs, and are connected by GB segments (edges) as illustrated in Fig. 2. The details of node placement and density for our particular examples are discussed in Section 3.2. In addition to the standard nodes, we create a supernode on one side of the microstructure that represents a diffusion source (node a in Fig. 2) and another supernode on the opposite side representing a diffusion sink (node b in Fig. 2). These supernodes span the entirety of their respective side of the sample and have many edges, whereas normal nodes in these GBNs possess only 2 or 3 edges. We use periodic boundary conditions in the direction orthogonal to the macroscopic flux (i.e. GBs that exit the top of the microstructure re-enter at the bottom with identical diffusivity so that flux across the periodic boundary is continuous).

By exploiting an analogy with electrical resistor networks [37, 38], the effective diffusivity of an arbitrary GBN can be expressed as:

$$D_{\text{eff}} = \frac{L}{A}\left[(\mathbf{e}_a - \mathbf{e}_b)^T \mathcal{L}^+ (\mathbf{e}_a - \mathbf{e}_b)\right]^{-1} \tag{1}$$

In Eq. 1, $\mathbf{e}_a$ is a vector who's a-th element (corresponding to the index of the source supernode) is equal to 1 and all others are 0, $\mathbf{e}_b$ is defined similarly. L and A are the sample length and cross-sectional area, respectively (without loss of generality, we assume the sample to be square with some out-of-plane thickness H so that $A = LH$). For the present work we considered microstructures with $L = 1$ mm, $H = 0.1$ mm, and $A = 0.1$ mm^2. The superscript ^{T} denotes the usual transpose operation. The superscript $^+$ indicates the Moore-Penrose pseudoinverse of the matrix $\mathcal{L}$, where $\mathcal{L}$ is the weighted Laplacian of the GBN graph. $\mathcal{L}$ encodes the topology of the GBN and the properties of each GB. With edge weights defined as $W_{ij} = D_{ij}A_{ij}/L_{ij}$, the elements of $\mathcal{L}$ are given by

$$\mathcal{L}_{ij} = \begin{cases} \sum_{i\sim m} D_{im}A_{im}/L_{im} & \text{if } i = j \\ -D_{ij}A_{ij}/L_{ij} & \text{if } i \sim j \\ 0 & \text{otherwise} \end{cases} \tag{2}$$

where D_{ij}, A_{ij}, and L_{ij} are, respectively, the diffusivity, cross-sectional area, and length of the edge connecting nodes i and j, with $i \sim m$ indicating that an edge exists between nodes i and m (i.e. the summation is over all nodes directly connected to node i). For the present work, we assumed a uniform GB width of 0.5 nm, and an out-of-plane thickness of $H_{GB} = H = 0.1$ mm, leading to a uniform GB cross-sectional area of $A_{ij} = 5 \times 10^{-14}$ m^2 $\forall$ $(i, j) \in E$. The matrix $\mathcal{L}$ is real and symmetric and can be decomposed according to

$$\mathcal{L} = U\Lambda U^{-1} \tag{3}$$

where Λ is the diagonal matrix of eigenvalues ($\Lambda_{ij} = \lambda_i\delta_{ij}$) and U is the matrix whose columns are the eigenvectors of $\mathcal{L}$. Introducing Eq. 3 into Eq. 1 and simplifying we obtain, in summation notation,

$$D_{\text{eff}} = \frac{L}{A}\left(\sum_{k>1} \lambda_k^{-1}[u_k(a) - u_k(b)]^2\right)^{-1} \tag{4}$$

In this expression λ_k is the k-th eigenvalue of $\mathcal{L}$ and $u_k(a)$ and $u_k(b)$ are, respectively, the a-th and b-th elements of the k-th eigenvector, with a and b being the indices of the source and sink nodes, respectively. By convention, the eigenvalues are sorted such that $0 = \lambda_1 \leq \lambda_2 \leq \cdots \leq \lambda_K$, where K is equal to the number of nodes in the graph (i.e. the cardinality of V, sometimes denoted $|V|$). Eq. 4 allows us to compute the effective diffusivity of the GBN from the eigenvalues and eigenvectors of its corresponding graph representation.

An important feature of the SGT approach and the spectral expression embodied in Eq. 4 is that it permits us to decompose the structure of the GBN into its fundamental structural "frequency" and higher-order "over-tones" with respect to the property of interest (D_{eff}). Consider the approximation obtained using only the dominant (largest) term of this series, whose spectral index we will denote $\tilde{k}$:

$$\widetilde{D}_{\text{eff}} = \frac{L}{A}\frac{\lambda_{\tilde{k}}}{[u_{\tilde{k}}(a) - u_{\tilde{k}}(b)]^2} \tag{5}$$

Because all of the terms in Eq. 4 are non-negative, Eq. 5 represents a lower-bound on the effective diffusivity. It is worth noting that Eq. 5 is a homogenization relation for GBNs that allows the prediction of the effective diffusivity of a GBN, requiring only 3 microstructure dependent numbers: $\lambda_{\tilde{k}}$, $u_{\tilde{k}}(a)$, and $u_{\tilde{k}}(b)$. We hypothesize that the eigenvalue and eigenvector corresponding to the dominant term encode the microstructural features that govern the effective response of the GBN. The dominant eigenvalue and eigenvector of the GBN provide natural and flexible structural metrics that highlight the microstructural features that control the property of interest.

To test this hypothesis we generated a large number of distinct microstructures, constructed the GBN laplacian ($\mathcal{L}$) of each, computed all of the corresponding eigenvalues and eigenvectors, computed D_{eff} and $\widetilde{D}_{\text{eff}}$, and explored the possibility of a correlation between the dominant eigenvector and structural features in the GBN.

Before describing the technical details of the numerical implementation, it is instructive to note the similarities and differences between the SGT approach presented here and prior art. The derivation leading to Eq. 1 is implicitly based on a finite volume scheme with the assumption of linear profiles between one-dimensional cell centroids, and employing Neumann boundary conditions. Consequently, the discretization of the GBN domain is reminiscent of the finite volume method[1] (FVM), as well as related numerical methods for solving partial differential equations such as the finite element method (FEM) and the finite difference method (FDM). Indeed, any of these techniques could be used to solve the diffusion equation in order to obtain an approximation to the concentration field (i.e. the concentration at each node in the GBN). However, the present work is not concerned with determining nodal concentrations, rather our object is homogenization: evaluating the effective diffusivity of a heterogeneous domain (the GBN). While these methods could also be employed for this purpose, they would require the indirect multi-step process of computing the macroscopic flux from the nodal concentrations and subsequently the effective diffusivity as the ratio of the magnitudes of the flux and macroscopic concentration gradient. In contrast, the SGT approach computes the effective diffusivity in a single step, directly from $\mathcal{L}$, and is, therefore, ideally suited to the task of GBN homogenization.

Another significant difference is in the manner that the eigenvalues and eigenvectors of $\mathcal{L}$ are employed and interpreted. The definition of a matrix like $\mathcal{L}$ is not entirely unique to the SGT method described in the present work, as techniques such as FVM, FEM, and FDM also result in systems of equations that define characteristic system matrices (e.g. the system stiffness matrix in the FEM). Eigenvalues and eigenvectors of such system matrices have also been considered, e.g. in FEM the ratio of the extremal eigenvalues (largest to smallest) provides the condition number, which is used in error estimation [39–41]. It is worth noting that system stiffness matrices of fully constrained FEM models are invertible [40], whereas $\mathcal{L}$ is, by definition, singular (hence the Moor-Penrose pseudoinverse in Eq. 1) [38]. A key difference between prior art and the present work is that rather than being concerned with the largest or smallest eigenvalues of the system matrix (and their corresponding eigenvectors), we find that the eigenvalues and eigenvectors most relevant to the homogenization problem are those that correspond to the largest terms in Eq. 4—which, in contrast, we have observed to always be intermediate eigenvalues of $\mathcal{L}$—and we demonstrate how these can be used as metrics to characterize GBN structure through connection with ideas from spectral graph partitioning. We show that this novel approach yields new physical insight into the role of GBs with intermediate properties (Section 4.1), the existence and nature of a network scale structural transition (Sections 4.3–4.4), and the influence of triple junction characters on network connectivity (Section 4.5).

3.2 Generation of Synthetic Microstructures

GBN templates were first constructed via a 2D isotropic front-tracking grain growth code written by Jeremy Mason[2]. The density and position of the nodes are determined by this code, with nodes located at each TJ and additional nodes located along GBs. The density of the GB nodes is larger over regions of higher curvature. A total of 1771 distinct microstructures were generated, each containing between 99 and 100 grains.

[1] Though a full numerical convergence analysis is beyond the scope of the present study, this suggests that the sensitivity to discretization density should be similar to that of FVM.

[2] The code is based on the algorithm of [42], and is available at http://web.boun.edu.tr/jeremy.mason/documents/FTGG2_v1_0.zip

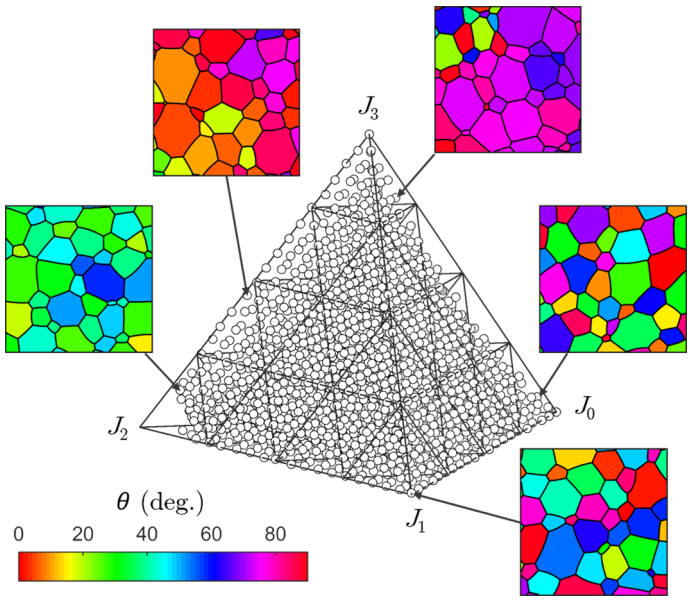

Figure 3: The TJ fraction (J_i) configuration space with representative microstructures indicated. Grains are colored by their crystallographic orientation, θ. The images shown here are magnified subregions of larger microstructures for the sake of visibility (i.e. there were more grains in the actual microstructures than are shown here).

The grains in these microstructures possessed cubic crystal symmetry and shared a common $\langle 001 \rangle$ rotation axis so that orientations were characterized by a scalar, $\theta \in [0°, 90°]$. This construction results in microstructures exhibiting perfect fiber textures, similar to those frequently considered in computational work [16, 18, 25, 26, 43–45], which, although difficult to synthesize experimentally, have the advantage that all of the resulting GBs exhibit exclusively tilt character by construction and, as described in Section 3.3, this facilitates connection with experimentally observed structure-property trends for GB diffusivity (trends in diffusivity over the full 5D GB character space have not yet been fully characterized). Grain orientations were assigned using the following Simulated Annealing procedure. First, grains were assigned an orientation uniformly at random from $\theta \in U(0°, 90°)$. GB disorientation angles, which we denote ω, were then computed and, defining low-angle GBs (LAGBs) by $\omega \leq 15°$, TJ fractions [21–25] were also computed. The TJ fractions, $\{J_i \mid i \in \{0, 1, 2, 3\}\}$, denote the fraction of TJs in a particular microstructure that are coordinated by i LAGBs. Since, $J_i \in [0, 1]\ \forall\ i$ and $\sum_{i=0}^{3} J_i = 1$, the space of physically realizable TJ fractions corresponds to a 3-simplex (tetrahedron), as shown in Fig. 3. This space is analogous to a quaternary phase diagram: the vertices correspond to microstructures in which all TJs are of one type while points in the interior contain a mixture of each type. This space was discretized into bins of width 0.05, resulting in a total of 1771 bins. After the initial random assignment of grain orientations, a microstructure was driven to one of these bins by allowing the reassignment of the orientation of a randomly selected grain at each Monte Carlo step. Reassignments that lowered the difference between the instantaneous $\{J_i\}$ and the target $\{J_i\}$ were always accepted, while reassignments that increased this difference were accepted with a finite probability that decreased with each step, similar to the methods used in [46]. One microstructure was driven towards each of the 1771 bins. However, as has been noted in [47], some locations in this space are difficult or impossible to reach with finite sized microstructures (e.g. a microstructure composed exclusively of J_0 and J_3 type TJs is topologically frustrated and can only be constructed in the limit of an infinite microstructure). Consequently, some destinations were not reached and the microstructures driven towards them instead converged to nearby bins. Using this procedure we generated microstructures that spanned the majority of the triple-junction space (see Fig. 3). Because the $\{J_i\}$ encode local correlations, this allowed us to

test our hypothesis on a diverse set of microstructures whose GBN structures and effective properties varied dramatically.

3.3 Constitutive Equations

After each microstructure was generated, GBs were assigned a diffusivity based on their disorientation angle according to one of two types of constitutive equations shown in Fig. 4. Figure 4a is a step function approximation that is often employed in simulations [44, 45, 48–52], and which we refer to as the *bichromatic* (i.e. binary) constitutive model. Figure 4b is a continuous function similar in form to what is observed in both experiments and simulations for ⟨001⟩ tilt GBs in FCC metals [53, 54] (all GBs in our microstructures are tilt GBs by construction). Because the constitutive equations used in the present work depend only on disorientation angle (not GB plane) the subtle asymmetry about $\omega = 45°$ that is observed in experiments is not present. This simplification is not essential, and the methods presented here are compatible with arbitrary constitutive models (e.g. the dependence on GB plane could be included if such a model was available). To explore the influence of property contrast (i.e. the ratio of the maximum to minimum diffusivity), we tested three different contrast ratios: $D_{\text{high}}/D_{\text{low}} \in \{10^1, 10^3, 10^7\}$.

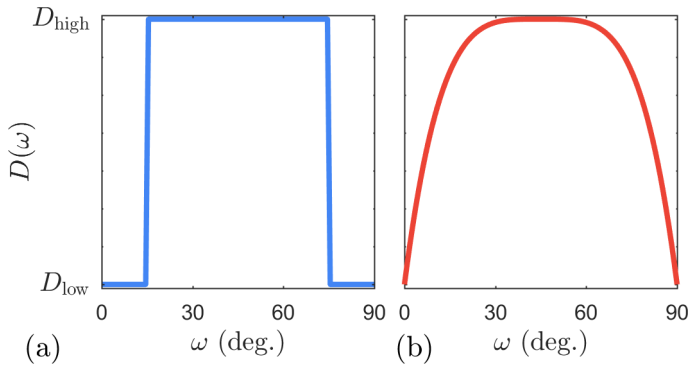

Figure 4: Constitutive equations used for GB diffusivity. Vertical axis is logarithmically scaled.

With diffusivities assigned to each edge, Eq. 2 was used to construct the corresponding diffusivity-weighted GBN Laplacian. The eigenvectors and eigenvalues were then computed and Eqs. 4–5 were used to compute the exact and approximate effective diffusivities of each microstructure respectively.

4 Results & Discussion

4.1 Homogenization for GBNs

Few homogenization relations for defect sensitive properties exist [55]. Previous work on GBN diffusivity has employed effective medium theory (EMT) [15, 16, 45], percolation theory (PT) [45], and the generalized effective medium (GEM) equation [45, 51, 52]. EMT provides useful results when the property contrast is low or the microstructures under consideration do not contain a percolating path of high-diffusivity boundaries. PT models apply when the property contrast is high and when the spectrum of GB types can reasonably be appoximated as bichromatic (i.e. consisting of only two types of GBs). The GEM is a phenomenological model that combines elements of EMT and PT and provides accurate results across a broad range of contrast ratios for bichromatic constitutive models [45]. Although less studied, polychromatic and multicomponent percolation models have been developed to investigate transport in the presence of a system composed of a finite number of component types [56–60]. A polychromatic percolation model was developed and applied to the problem of GBN diffusivity by Chen & Schuh [45].

It has been observed in simulations that the location of the percolation threshold is sensitive to correlations that exist in real microstructures, and this is not captured by classical PT models. Previous work has demonstrated how sensitivity to local correlations may be incorporated into the GEM [51, 52], and accurate predictions were obtained for certain classes of microstructures. However, predicting effective diffusivity in the vicinity of the percolation threshold remains challenging for general microstructures.

In what follows, we demonstrate that the SGT approach presented in this paper provides a homogenization equation for GBN diffusivity (Eq. 5) that yields accurate predictions for both bichromatic and continuous constitutive models over a broad range of property contrast ratios and microstructural correlations.

For the bichromatic constitutive model, the predictions of the 1-term SGT approximation from the present work (Eq. 5) are shown in Fig. 5a. The agreement is excellent for all of the microstructures (below, at, and above the percolation threshold). For the continuous constitutive model, which is a better representation of true GB structure-property relations, the performance of the 1-term SGT predictions were also found to be excellent across a wide range of property contrast ratios (Fig. 5b). Because Eq. 5 is a lower-bound, all of the deviation is to the left of the red lines (coincidence with the red lines would indicate perfect agreement).

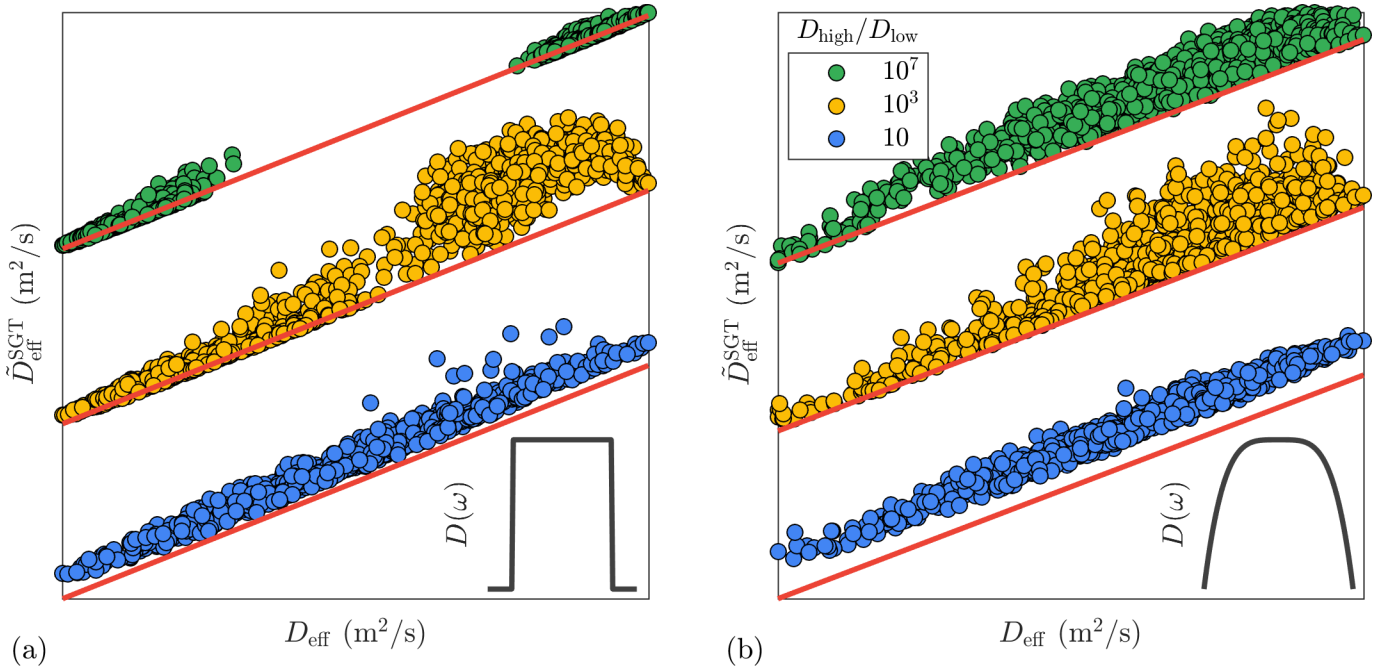

Figure 5: Comparison of 1-term SGT predictions ($\widetilde{D}_{\text{eff}}^{SGT}$) from Eq. 5 to actual effective diffusivity (D_{eff}) for all 1771 microstructures using (a) the step function constitutive equation (shown in inset) or (b) the continuous constitutive equation (shown in inset) for three different contrast ratios (see legend). If agreement was perfect, all points would fall on the respective red lines. Axes are logarithmically scaled and values have been normalized and shifted vertically so that they could be plotted side by side for comparison (thus axis tick marks have been omitted).

For the oft-employed bichromatic constitutive model, the gap between percolating and non-percolating microstructures gradually disappeared as the property contrast ratio decreased. In comparison, the microstructures whose GBs were assigned diffusivities based on the more realistic continuous constitutive equation were not separated into percolating and non-percolating microstructures, but instead showed a continuous spectrum of effective diffusivities even at the highest contrast ratios (contrast ratios as high as $D_{\text{high}}/D_{\text{low}} = 10^{28}$ were tested with essentially identical results). This suggests that the presence of GBs with intermediate diffusivities can play a non-negligible role in determining the effective diffusivity

of a GBN, even when the property contrast is extremely high. We recommend, therefore, that future modeling efforts incorporate continuous or at least polychromatic constitutive models.

4.2 Dominant GBN Structural Features and Eigenvectors

It is useful to think of the eigenvectors of the GBN, $\mathbf{u}_k$, as being analogous to the eigenmodes of a vibrating string. The eigenvector corresponding to the dominant term in Eq. 4, denoted $\mathbf{u}_{\tilde{k}}$, can be thought of abstractly as the eigenfunction, $u_{\tilde{k}}(v)$ with $v \in V$, representing the dominant structural "vibration" (i.e. the dominant eigenmode) of the GBN. In other words, it encodes the structural features of the GBN that dominate the effective response of the network: D_{eff} in the present case.

Visualization of $\mathbf{u}_{\tilde{k}}$ therefore provides insight into what structural characteristics of a GBN govern its aggregate behavior. Two representative examples for the bichromatic constitutive model are instructive. Figure 6a shows a visualization of $\mathbf{u}_{\tilde{k}}$ for a microstructure that does not percolate and consequently has a low D_{eff}. The height and color of node v is given by the value of the v-th element of $\mathbf{u}_{\tilde{k}}$. The smooth sinusoidal appearance is characteristic of microstructures below the percolation threshold, which are relatively homogeneous, and for which the eigenvector shows a gradual transition because its value at any given node is very similar to that of its neighbors.

Figure 6b shows a visualization of $\mathbf{u}_{\tilde{k}}$ for a microstructure above the percolation threshold. In this case there are large differences between the values of $\mathbf{u}_{\tilde{k}}$ at adjacent nodes and the trend is not smooth in many places. The region of gradual transition is restricted to what appears to be a narrow path connecting one side of the microstructure to the other, as is characteristic of the other percolating microstructures we have observed.

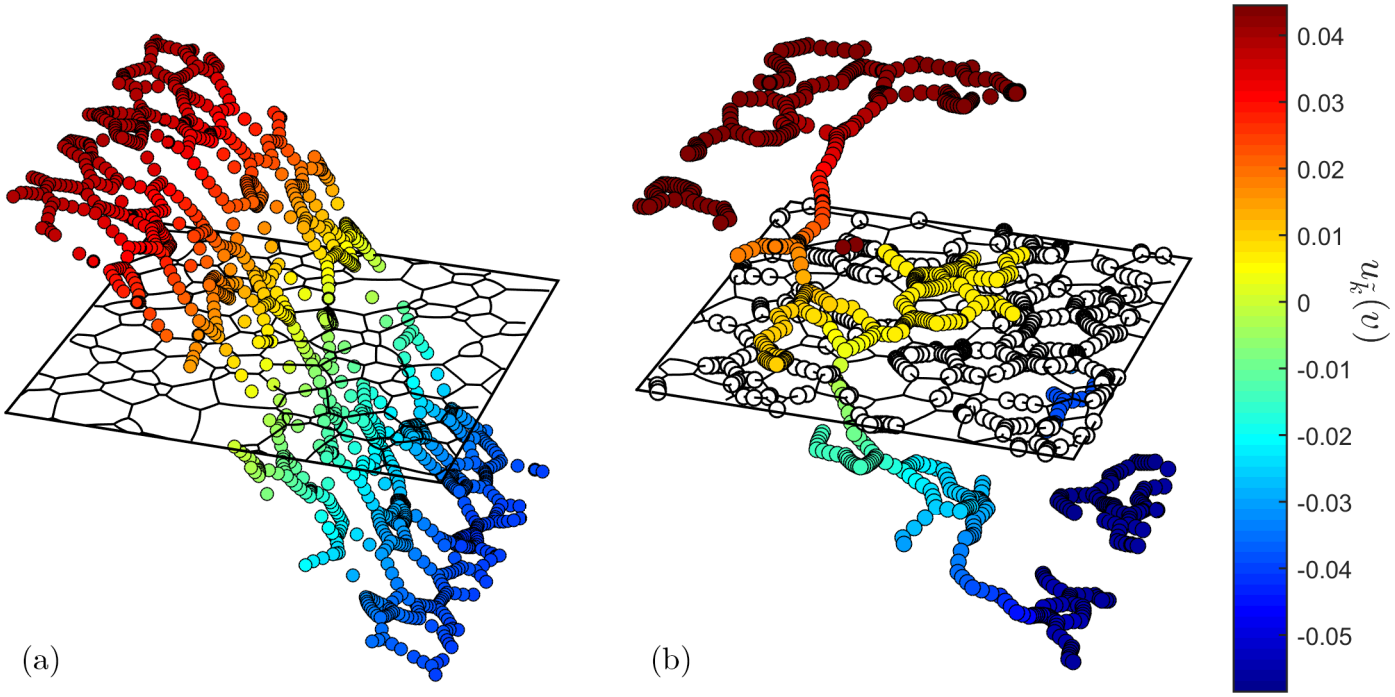

Figure 6: Plot of $u_{\tilde{k}}(v)$ for GBNs (a) below and (b) above the percolation transition, respectively. The color and height of node v are given by $u_{\tilde{k}}(v)$. For the sake of visual clarity, the nodes in (b) whose values are very close to zero are not colored.

Figure 7 identifies this path with the percolating cluster of high-angle—and therefore high-diffusivity—GBs (recall that the microstructure is periodic in the vertical direction). Not all of the high-diffusivity GBs are highlighted by $\mathbf{u}_{\tilde{k}}$, as evidenced by the disconnected cluster of HAGBs on the right, because

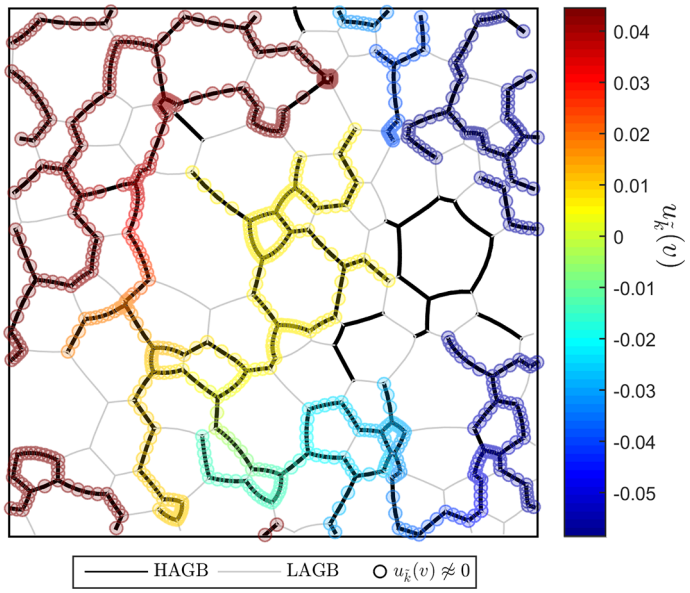

Figure 7: Top view of Fig. 6b with HAGBs and LAGBs indicated. For the sake of visual clarity, the nodes whose values are very close to zero are not shown.

these do not contribute strongly to the global diffusion. Thus, the dominant eigenvector, $\mathbf{u}_{\tilde{k}}$, is able to highlight the dominant feature of the GBN—which in this case happens to be a percolating cluster of high-diffusivity GBs—that contributes to the phenomenon under investigation.

4.3 A General Structure Metric for GBNs

For the high-contrast bichromatic constitutive model, the microstructures were well separated into two clusters: those that percolate (having high D_{eff}) and those that do not percolate (having low D_{eff}) (see Fig. 5). For this case nearly all (97%) of the non-percolating microstructures had $\tilde{k} = 2$ as their dominant term. All but one of the percolating microstructures (99.9%) had $\tilde{k} > 2$. The one exception was a microstructure for which all GBs are of type D_{high}, which is structurally equivalent to a microstructure for which all GBs are of type D_{low}, just having its GB properties (and consequently D_{eff}) modified by a scaling factor. Thus, the index of the dominant term, $\tilde{k}$, can distinguish between structurally dissimilar GBNs—those that percolate and those that do not—in the bichromatic case.

In the continuous case the gap between high diffusivity and low diffusivity GBNs disappears (see Fig. 5b). However, $\tilde{k}$ still encodes important structural information, though it is more complex and nuanced. The results presented in this section employ the continuous high-contrast ($D_{\text{high}}/D_{\text{low}} = 10^7$) constitutive equation. Because the number of nodes is not constant for all GBNs, it is useful to define a normalized spectral index, $\tilde{k}' = (\tilde{k} - 1)/(K - 1)$. As the GB diffusivity distribution is no longer binary, we also examine the entire distribution[3], $\rho[\log(D)]$, for each microstructure and characterize it by its length-weighted median. For a GBN possessing $|E|$ edges (GB segments), with the i-th GB segment having log-diffusivity $\log(D_i)$ and length L_i, sorted such that $\log(D_1) \leq \log(D_2) \leq \cdots \leq \log(D_{|E|})$, the

[3]We use $\rho[x]$ to denote the probability density of x. Also, $\log(x)$ will denote the base-10 logarithm.

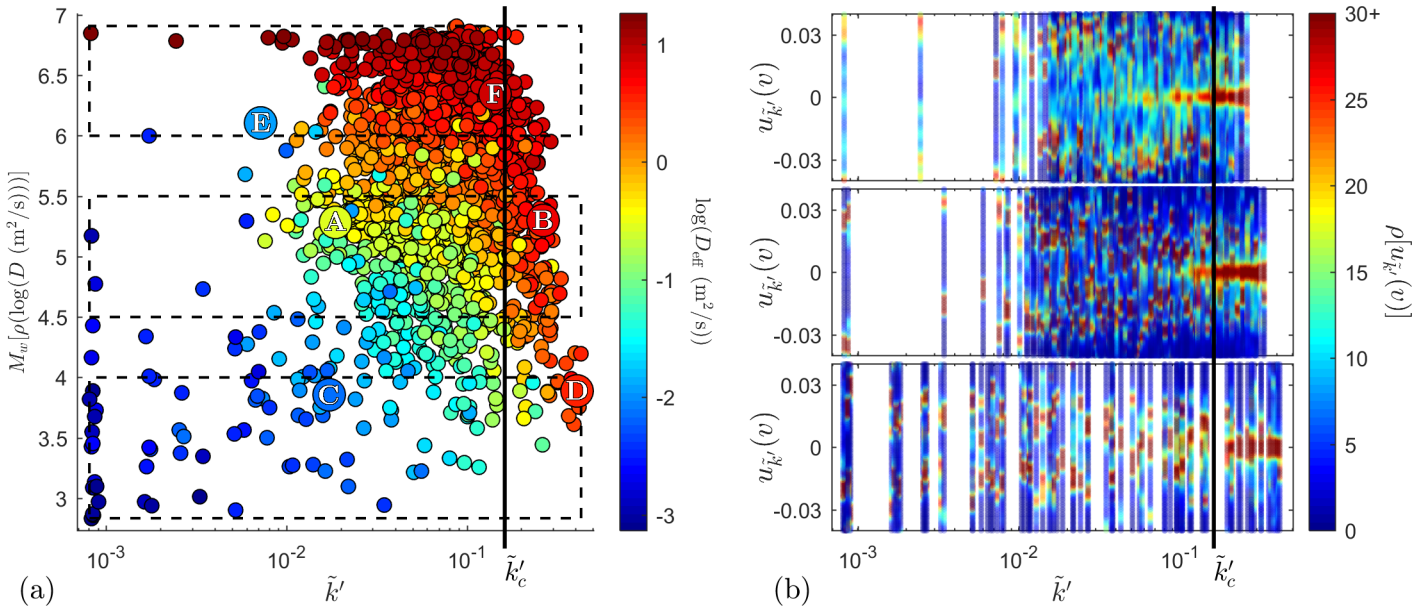

Figure 8: In (a) the variation in D_{eff} with changes in $\tilde{k}'$ and $M_w(\rho[\log(D)])$ is shown. Representative microstructures A-F are indicated as well as the approximate location ($\tilde{k}'_c$) of the GBN structural transition. The distributions, $\rho[u_{\tilde{k}'}(v)]$, for each of the microstructures contained in the three rectangular regions in (a) are shown in the corresponding subplots in (b) as generalized spectrograms where color indicates probability density. A gradual transition from bimodal to unimodal distributions in the vicinity of $\tilde{k}'_c$ is evident.

length-weighted median, denoted $M_w(\rho[\log(D)])$ is the element $\log(D_m)$ satisfying:

$$\sum_{i=1}^{m} L_i > \frac{1}{2}\sum_{i=1}^{|E|} L_i \tag{6}$$

$$\sum_{i=m}^{|E|} L_i \geq \frac{1}{2}\sum_{i=1}^{|E|} L_i \tag{7}$$

Figure 8a provides a scatter plot of $M_w(\rho[\log(D)])$ vs. $\tilde{k}'$ with markers colored by $\log(D_{\mathrm{eff}})$. We observe the following trends: first, as $M_w(\rho[\log(D)])$ increases (i.e. as $\rho[\log(D)]$ shifts towards higher $\log(D)$) the effective diffusivity increases, as would be expected; second, as we observed earlier in the binary case, higher spectral indices are associated with increased connectivity of high-diffusivity GBs and consequently higher D_{eff}. Points labeled A-D in Fig. 8 correspond to microstructures with various values of $\tilde{k}'$ and $M_w(\rho[\log(D)])$ and are chosen to illustrate important GBN structural differences. Figure 9 shows $u_{\tilde{k}'}(v)$ for microstructures A-D (in color) as well as their respective GBNs with GBs colored according to their diffusivity (in grayscale). The distributions $\rho[u_{\tilde{k}'}(v)]$, and $\rho[\log(D)]$ are also provided in the corresponding colorbars.

Microstructure A exhibits an abrupt spatial transition in the values of $u_{\tilde{k}'}(v)$ from a broad plateau of nodes having values $u_{\tilde{k}'}(v) \approx 0.016$ to a plateau of $u_{\tilde{k}'}(v) \approx -0.008$. As shown in the adjacent image of $\log(D)$, the location of this sudden change corresponds to the position where the left and right portions of the GBN are separated by GBs all having lower values of diffusivity. We observe that large gradients in $u_{\tilde{k}'}(v)$ are correlated with bottlenecks for diffusive transport (i.e. GBs with low diffusivity) whereas small gradients are indicative of easy transport paths. Microstructure C, which has a low value of $\tilde{k}'$ similar to that of microstructure A (but with a diffusivity distribution containing fewer high diffusivity GBs), likewise shows an abrupt spatial transition in $u_{\tilde{k}'}(v)$ corresponding to a band of lower diffusivity

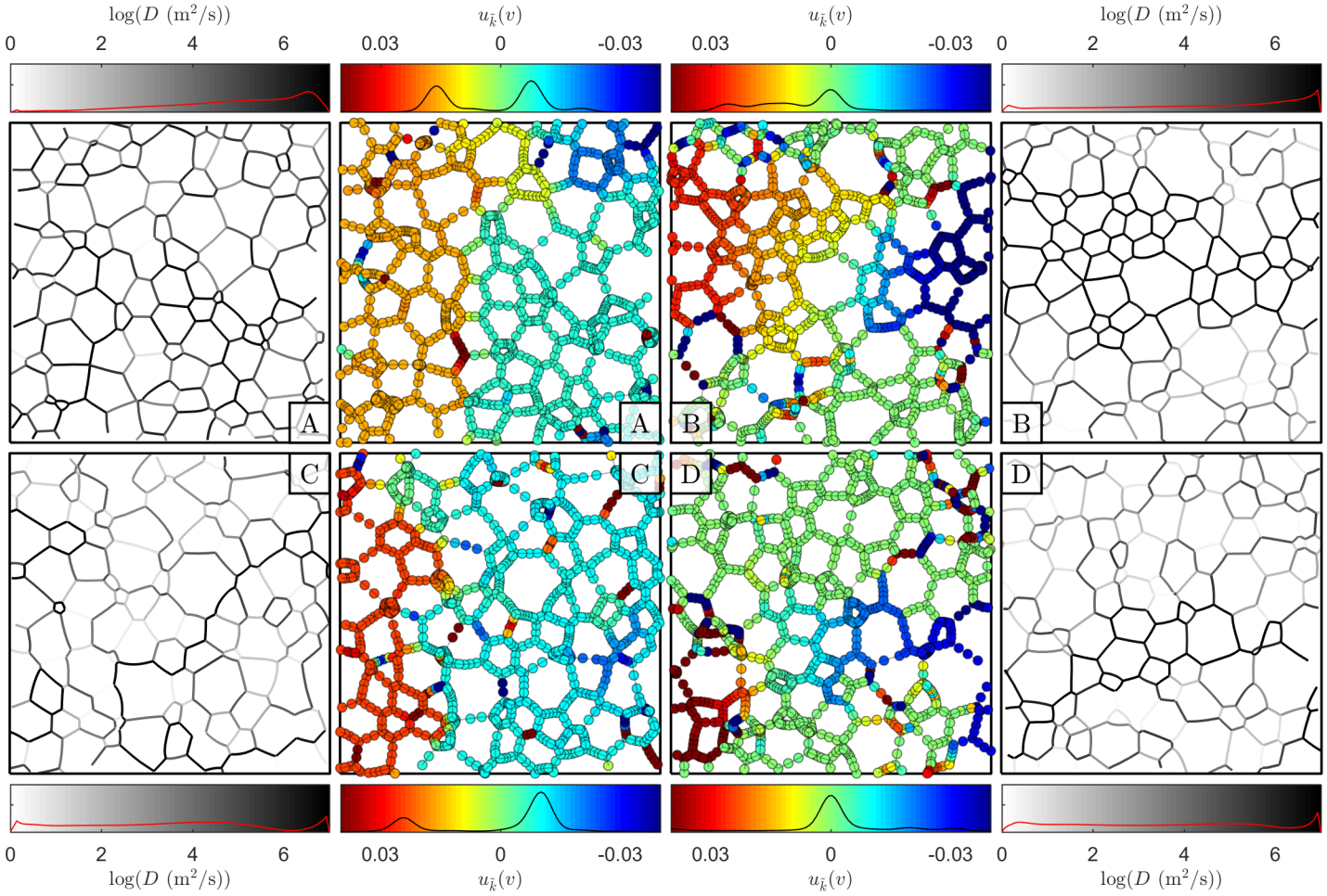

Figure 9: For microstructures A-D from Fig. 8, plots of $u_{\tilde{k}'}(v)$ are shown (in color), as well as the respective GBNs with GBs shaded by $\log(D)$ (in grayscale). The distributions $\rho[u_{\tilde{k}'}(v)]$ and $\rho[\log(D)]$ are shown in the respective colorbars, with the scale of the vertical axes identical across all of the microstructures to facilitate direct comparison.

GBs separating opposing sides of the microstructure in the direction of flux. Although their $\log(D)$ distributions differ, the dominant structural characteristic of their GBNs is similar, as captured by their similar values of $\tilde{k}'$.

This signature of the dominant structural feature of these GBNs is also manifest in the distribution $\rho[u_{\tilde{k}'}(v)]$ (shown in the corresponding colorbars) as two well-separated peaks that correspond to these weakly connected subpopulations of nodes. In contrast, the GBNs of microstructures B and D, which are both characterized by much larger values of $\tilde{k}'$, show a gradual transition in the values of $u_{\tilde{k}'}(v)$ across the microstructure, corresponding to a connected path of relatively high diffusivity GBs (note the location of the connected paths of GBs with high $\log(D)$ that span the microstructures). A signature of this type of GBN structure is also evident in the distribution $\rho[u_{\tilde{k}'}(v)]$, which has its density concentrated around $u_{\tilde{k}'}(v) = 0$. This characteristic difference in $\rho[u_{\tilde{k}'}(v)]$ is related to graph theoretic techniques used for spectral graph partitioning [32, 61–65] and image segmentation [64, 66]. Images or graphs for which the elements of the relevant eigenvector are distributed as well-separated subpopulations are easily partitioned/segmented. For GBNs this scenario corresponds to microstructures that are weakly connected and therefore have low values of D_{eff} (microstructures A and C). Microstructures (or images) like B and D, which do not exhibit well separated subpopulations of eigenvector elements are more connected (and hence do not partition well) and have increased D_{eff}.

The characterization of GBNs by their spectral index $\tilde{k}'$ and $\rho[u_{\tilde{k}'}(v)]$ provides a more general and

flexible measure of network connectivity than has previously been available. Although GB clusters have been examined previously by employing concepts from percolation theory (e.g. cluster mass, radius of gyration) [18, 67], these methods rely on the binary characterization of GBs as "special" or "general" (i.e. one examines the sizes of clusters of "special" boundaries). In the context of a continuous distribution of GB types the definition of a cluster becomes less straightforward (where does one cluster end and another begin?). The SGT metrics proposed here resolve this issue by effectively performing the clustering in the space of the eigenvector elements, via the peaks/subpopulations revealed in $\rho[u_{\tilde{k}'}(v)]$, rather than attempting to cluster discrete GB types in the space of the physical microstructure. Metrics that rely on binary GB classification are well suited to answer the question of *whether* a particular type of GB forms a sample spanning connected cluster. In contrast, the SGT metrics are capable of characterizing *the degree of global network connectivity.*

4.4 A GBN Structural Transition

The fundamental change in the distribution $\rho[u_{\tilde{k}'}(v)]$ with increasing $\tilde{k}'$ is indicative of a GBN structural transition and can be observed more generally, as shown in Fig. 8b. Each of the subplots in Fig. 8b correspond to the microstructures contained in the adjacent rectangles in Fig. 8a and are separated into three groups for clarity. It is apparent that as $\tilde{k}'$ increases there is a transition from well-separated multimodal distributions to approximately unimodal distributions centered at $u_{\tilde{k}'}(v) = 0$. This transition is gradual and may have a slight dependence on $M_w(\rho[\log(D)])$, but is largely complete above a value of $\tilde{k}'_c \approx 0.1827$.

To investigate the impact of this GBN structural transition on the effective property D_{eff}, we identified subsets of GBNs with approximately identical distributions of GB types (i.e. $\rho[\log(D)]$)—so as to isolate the effect of the structural transition—and observed changes in D_{eff} with increasing $\tilde{k}'$. To identify sets of GBNs with similar $\rho[\log(D)]$, we used Affinity Propogation (AP) [68], where the negative Jensen–Shannon Divergence (JSD) [69], defined for the present case by

$$-\text{JSD}(\rho_i[\log(D)]\|\rho_j[\log(D)]) = -\frac{1}{2}\int_0^\infty \rho_i[\log(D)]\log\left(\frac{2\rho_i[\log(D)]}{\rho_i[\log(D)]+\rho_j[\log(D)]}\right) + \rho_j[\log(D)]\log\left(\frac{2\rho_j[\log(D)]}{\rho_i[\log(D)]+\rho_j[\log(D)]}\right)\text{d}(\log(D)) \tag{8}$$

was used as the similarity measure. Discretizing the domain of $\log(D)$, an approximation to the negative Euclidean distance (ED), $-\|\rho_i[\log(D)]-\rho_j[\log(D)]\| \approx \sqrt{\sum_{m=1}^{M}\left(\rho_i[\log(D_m)]-\rho_j[\log(D_m)]\right)^2}$, was also used as a similarity measure and the results were similar, though fewer sets (51) were obtained using the JSD compared with the ED (78), and the results shown here are from the JSD sets. To further verify the results we also created two new sets of microstructures using microstructures B and E from Fig. 8–11 as templates and applying simulated annealing to reassign grain orientations so that the resulting GBNs had values of $\tilde{k}'$ varying from 10^{-3} to 10^{-1}, while keeping the distributions $\rho[\log(D)]$ constant.

As illustrated in Figure 10 the onset of the GBN structural transition observed in $\rho[u_{\tilde{k}'}(v)]$ in the vicinity of $\tilde{k}'_c$ corresponds to a transition in D_{eff} from consistently low values below $\tilde{k}'_c$, to sharply increasing D_{eff} above it. This "critical" spectral index appears to play a role similar to the critical temperature in second-order phase transitions. This structural transition, while analogous to the percolation transition in bichromatic systems, is distinct in an important way: the transition is a continuous one. For bichromatic systems there is a discontinuous change in the effective properties of the system once the "infinite cluster" has formed, resulting in the distinct and well separated sets of percolating and non-percolating microstructures observed in Fig. 5a. In a sense, with sufficiently high contrast the bichromatic constitutive model approximately quantizes the effective properties of the system and there

Microstructure	p_{LAGB}	J_0	J_1	J_2	J_3	D_{eff} (m^2/s)
E	0.37	0.56	0.09	0.04	0.31	0.01
F	0.35	0.55	0.11	0.05	0.30	8.14

Table 1: The values of traditional GBN metrics for microstructures E and F, including the length-fraction of low-angle GBs, p_{LAGB}, and triple junction fractions, J_i. The effective diffusivity, D_{eff}, for each microstructure is also provided.

is a range of intermediate D_{eff} values that is not observed. However, in the context of a continuous spectrum of constituent (i.e. GB) properties, both connectivity and clusters, whether infinite or otherwise, are not well defined and the "phase transition" becomes continuous. We observe that, in both cases, the dominant spectral index, $\tilde{k}'$, provides a general structure metric for GBNs, analogous to a GBN order parameter, which encodes the global structure of the GBN and can be used to identify and characterize fundamental structural and property transitions in GBNs.

Our use of the term "structural transition" deserves some justification. Although it is more of a philosophical point than a technical one, we submit that from the perspective of the network the most relevant description of structure is the spatial distribution or connectivity of *properties*, rather than the connectivity of GBs of specific crystallographic characters. The properties of GBs are not monotonic functions of their crystallographic character over the full 5-dimensional space, rather there are many GBs whose crystallographic character is distinct (i.e. that are not symmetrically equivalent), but that exhibit essentially identical properties [53, 54, 70]. Such boundaries have an indistinguishable effect on the network and its effective properties. Consequently, we believe that, while certainly not the only tenable perspective, the description of the transition in GBN structure in terms of property connectivity is appropriate.

This is not to suggest that the crystallography is not important. On the contrary, the requirement of crystallographic consistency [71] may impose constraints on allowed network configurations [18] and consequently allowed spatial arrangements of properties. We investigate this affect and provide results from this perspective in Section 4.5.

4.5 Comparison with Traditional GBN Metrics

It is worth noting that the SGT metrics presented here, especially $\tilde{k}'$, are the first structure metrics for GBNs capable of simultaneously considering the realistic scenario of a continuous spectrum of GB properties as well as the correlations that exist in real GBNs. As a comparison, consider microstructures E and F (see Fig. 8), which have nearly identical fractions of low-angle grain boundaries and TJ fractions (see Table 1)—the traditional metrics for GBNs—and yet whose D_{eff} differ by more than 2 orders of magnitude. In contrast, the spectral index, $\tilde{k}'$, is very different for these two GBNs and thus captures the significant differences in their structure that are responsible for their widely varying properties. By comparing $\rho[u_{\tilde{k}'}(v)]$ of these two GBNs (see the distributions in the respective colorbars of Fig. 11) it is apparent that microstructure E and F are on opposite sides of the structural transition that occurs in the vicinity of $\tilde{k}'_c$ and their very similar property distributions, $\rho[\log(D)]$, but clearly distinct GBN structure, can be observed directly in Fig. 11.

At the same time, it is likely that there is some overlap in the structural information encoded by traditional metrics and the SGT metrics presented here and it is instructive to examine how they may be correlated. The most commonly used structural metrics for GBNs are the special fraction, p_{special}, which is the number- or length-fraction of "special" GBs, and the TJ fractions, $\{J_i \mid i \in [0,3]\}$, which were defined in Section 3.2. Both of these traditional metrics rely on a binary taxonomy of GBs as possessing either "special" or "general" character, where "special" is typically defined as either LAGBs

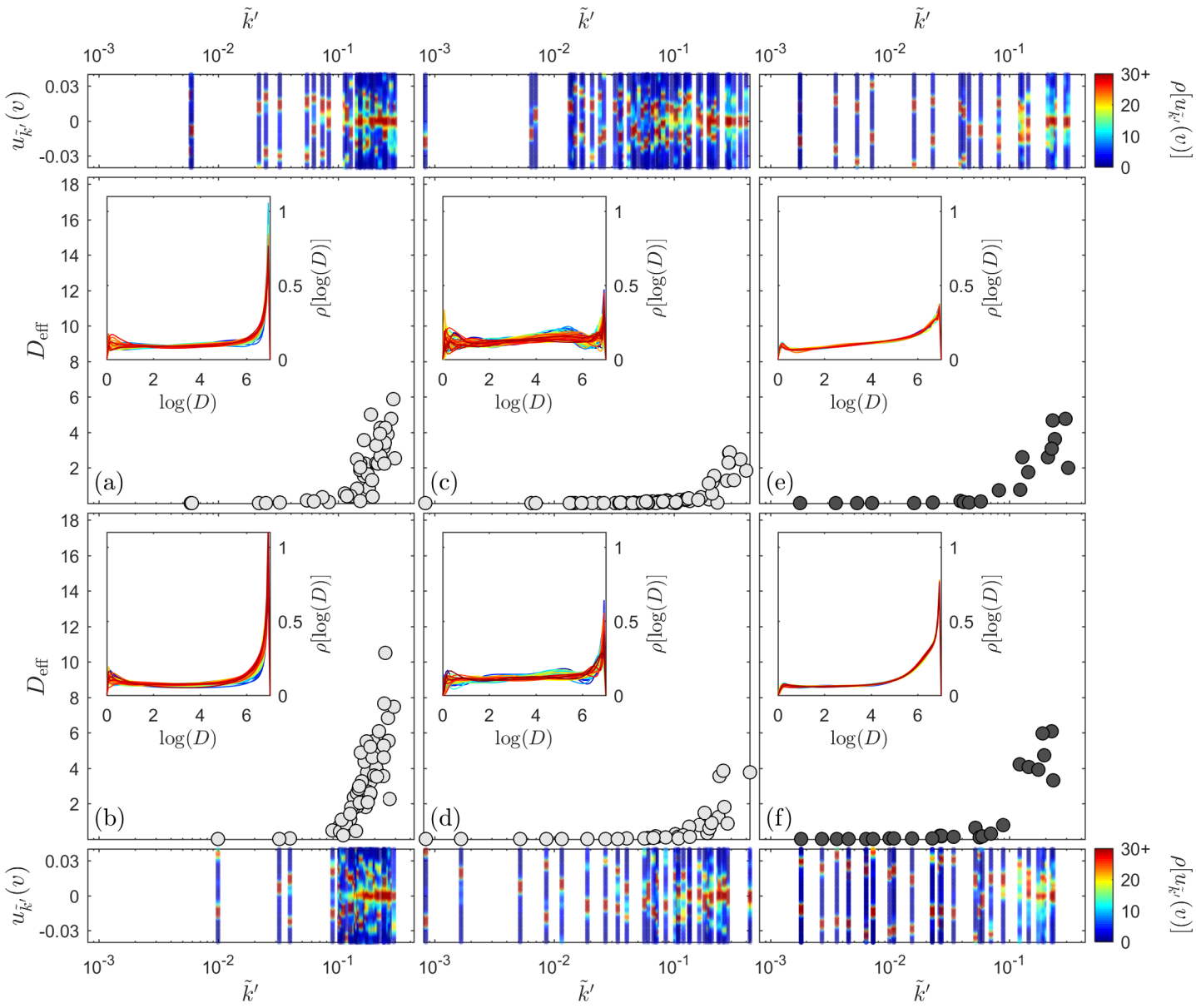

Figure 10: In (a)-(d) D_{eff} is compared to $\tilde{k}'$ for four different clusters of microstructures obtained using AP with negative JSD similarity measure. Plots of $\rho[\log(D)]$ are shown in the respective insets for each cluster, with the distribution for each microstructure plotted in a different color. Note the similarity in $\rho[\log(D)]$ within each cluster. The spectrograms of $\rho[u_{\tilde{k}'}(v)]$ for each cluster are also shown above/below the respective plot and colored in the same fashion as Fig. 8b. In (e)-(f) the same plots are given for the new sets of microstructures generated from microstructures B and E, respectively, using the simulated annealing procedure described in the text.

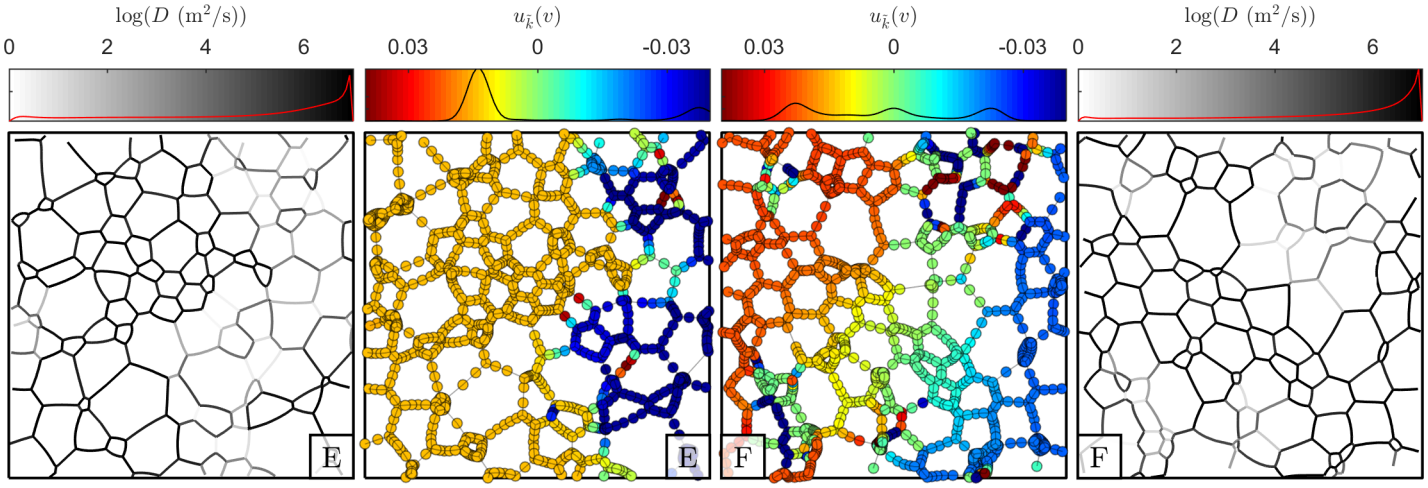

Figure 11: For microstructures E-F from Fig. 8, plots of $u_{\tilde{k}'}(v)$ are shown (in color), as well as the respective GBNs with GBs shaded by $\log(D)$ (in grayscale). The distributions $\rho[u_{\tilde{k}'}(v)]$ and $\rho[\log(D)]$ are shown in the respective colorbars, with the scale of the vertical axes identical to those from Fig. 9 to facilitate direct comparison.

or certain low-Σ coincident site lattice (CSL) boundaries. As p_{special} does not encode any connectivity information, we focus our comparison on the J_i. Figure 12 shows a plot of the J_i coordinates of all 1771 microstructures where the value of $\tilde{k}'$ for each microstructure is indicated by the corresponding marker color. Microstructures with $\tilde{k}' < \tilde{k}'_c$ are semi-transparent, while those with $\tilde{k}' > \tilde{k}'_c$ are fully opaque with black outlines to highlight the location of the GBN structural transition in this space. It is clear from Fig. 12 that $\tilde{k}'$ increases with decreasing J_2. This is sensible as J_2-type TJs are coordinated by 2 low-angle and, consequently, low diffusivity GBs making them bottlenecks for mass transport, so one would expect that fewer bottlenecks would lead to improved connectivity and consequently higher $\tilde{k}'$. However, the situation is not quite so simple, as illustrated in Fig. 13.

For a given value of J_2 a broad range of values of $\tilde{k}'$ are possible. This is because the TJ fractions are measures of *local* connectivity, whereas $\tilde{k}'$ encodes *global* connectivity. Consequently, there are many distinct GBN configurations having identical values of J_2—or even having the same amounts of each TJ type—but arranged in different spatial configurations. Likewise, a particular value of $\tilde{k}'$ can be achieved with a variety of different TJ fractions, i.e. the global connectivity encoded in $\tilde{k}'$ can be achieved in a variety of ways. However, there appears to be an upper bound on $\tilde{k}'$ that exponentially decays with increasing J_2 (see Fig. 13c). This suggests that while the local constraints imposed by the TJ fractions do not fully specify $\tilde{k}$, they do limit how globally connected the microstructure can be. The GBN structural transition that occurs in the vicinity of $\tilde{k}'_c$ can therefore be associated with a critical value of J_2, which we observe to be $J_{2,c} \approx 0.2703$. Microstructures with $J_2 > J_{2,c}$ are unlikely to have well-connected GBNs due to the effect of the corresponding local constraints on the global network structure.

Although the functional dependence is less obvious and not necessarily monotonic for the other J_i, these too appear to bound the possible values of $\tilde{k}'$. Since J_0-type triple junctions are coordinated by all high-angle GBs, one would assume that increasing J_0 would always lead to an increase in $\tilde{k}'$, but this is not the case. Instead $\tilde{k}'$ reaches a maximum around $J_0 = 0.25$ and then *decreases*. This highlights the fact that $\tilde{k}'$ is *not* measuring the connectivity of a particular type of GB (e.g. high-angle), rather it describes the network structure more generally. As J_0 increases, the microstructure begins to become saturated with high-diffusivity GBs and therefore becomes more homogeneous, that homogeneity is reflected in the lower values of $\tilde{k}'$ which indicate that the dominant microstructural features correspond to lower frequency GBN "vibrational" modes.

In contrast, the highest value of $\tilde{k}'$ is achieved for a microstructure composed primarily of a mixture

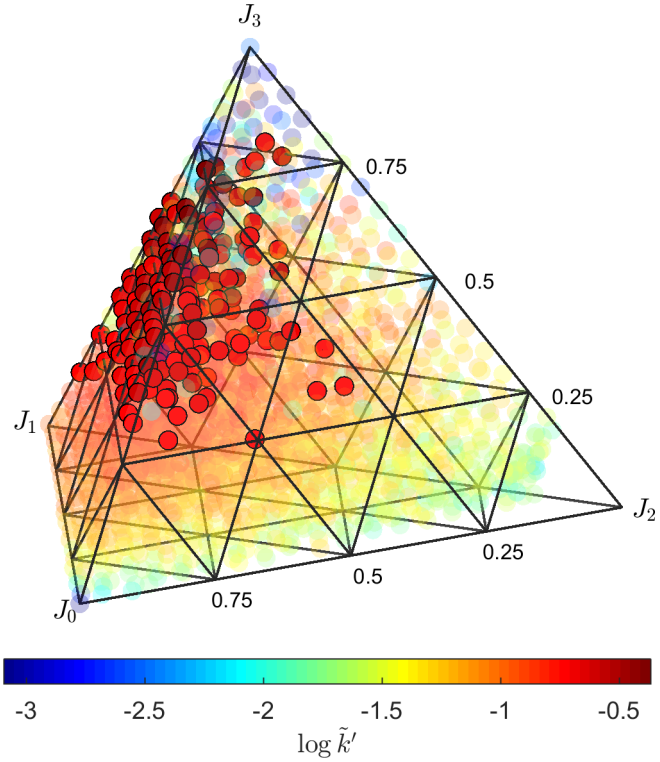

Figure 12: Comparison of $\tilde{k}'$ and J_i. The J_i coordinates of all 1771 microstructures are given with each marker colored by the value of $\tilde{k}'$ of the corresponding microstructure. Semi-transparent markers correspond to microstructures with $\tilde{k}' < \tilde{k}'_c$.

of J_0- and J_3-type TJs (specifically, $\{J_0, J_1, J_2, J_3\} = \{0.245, 0.105, 0.055, 0.595\}$), which leads to a very heterogeneous microstructure characterized by high frequency "vibrational" modes. In fact, as illustrated in Fig. 14 the GBN has essentially phase separated into a corridor of high-diffusivity GBs surrounded by a sea of comparatively low-diffusivity GBs. Since J_0- and J_3-type TJs cannot share a GB—in a sense they are insoluble GBN constituents—as the microstructure becomes dominated by these two types it must minimize the extent of the border between them. Indeed, a microstructure composed of only J_0- and J_3-type TJs can only be achieved in the limit of an infinite microstructure.

The results of Sections 4.3-4.5 suggest that $\tilde{k}'$ provides a quantitative measure of the degree of global connectivity and heterogeneity in GBNs in the context of continuous distributions of GB properties and the existence of microstructural correlations, and as such, is able to identify global transitions in network structure. This provides unique information beyond that of existing metrics and techniques, which either characterize local structure only (J_i), consider a finite number of discrete GB types (percolation theory), conflate connectivity and the distribution of GB types (critical path analysis [72]), or answer only the binary question of *whether* the network is connected (percolation theory).

5 Summary/Conclusions

In this paper we introduced the use of spectral graph theory (SGT) to the study of grain boundary networks (GBNs) in polycrystalline microstructures. The eigenvalues and eigenvectors of a diffusivity-weighted GBN Laplacian provide a set of SGT-based structural metrics to characterize the dominant structural features of GBNs.

In this context, we derived a series expression that provides a new homogenization (i.e. structure-property) relation for the effective diffusivity of a GBN. Requiring only 3 microstructure sensitive pa-

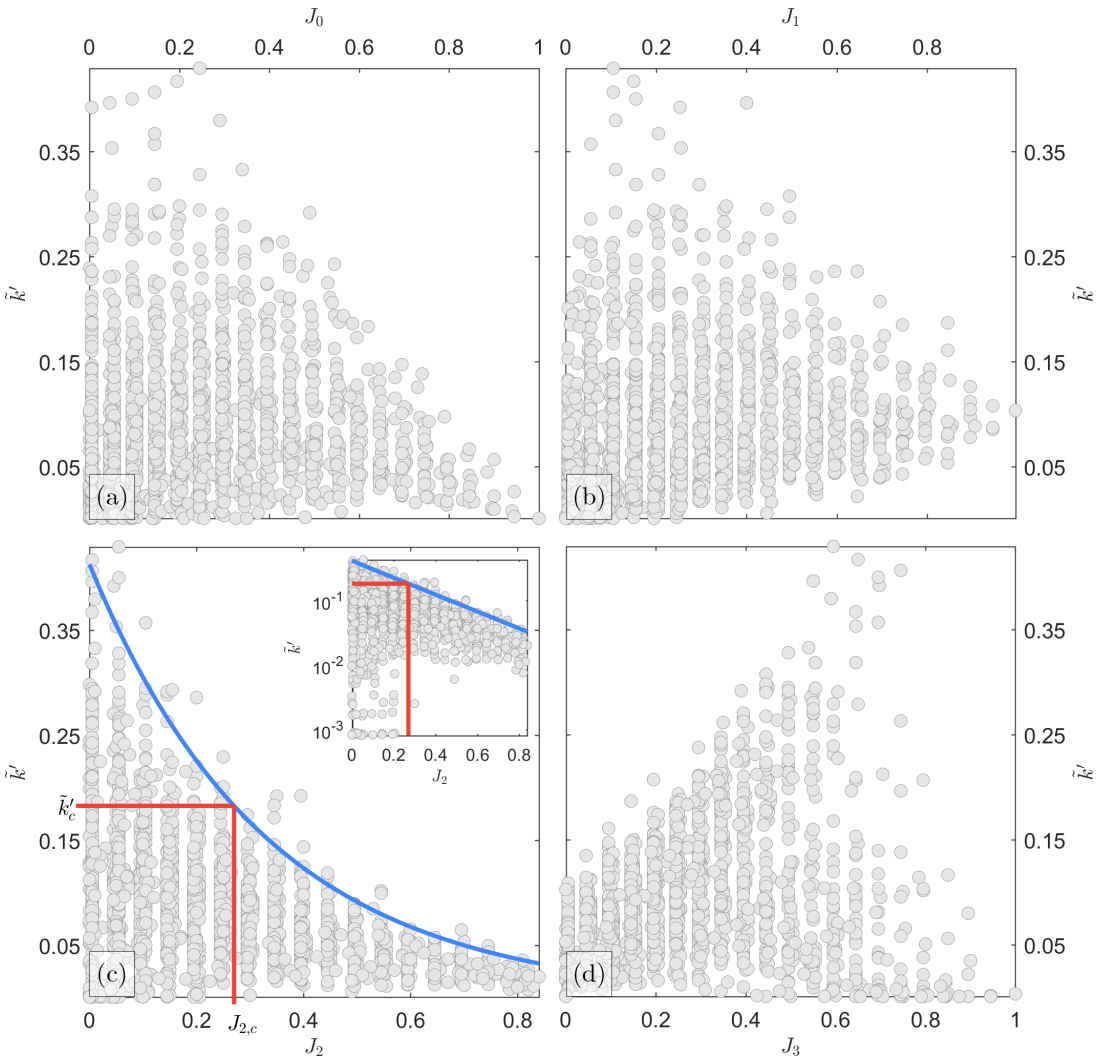

Figure 13: Plot of the spectral index ($\tilde{k}'$) vs. TJs fractions (J_i) for all 1771 microstructures. Inset shows the same data on a semi-logarithmic scale to emphasize the exponential decay of the upper bound. Blue curve is a visual guide to the upper bound corresponding to $\tilde{k}'_{\max} \approx \exp\left[-3.0144 J_2 - 0.8851\right]$. Red lines indicate the approximate position of the critical values $\tilde{k}'_c$ and $J_{2,c}$ respectively.

rameters, the dominant term of this series provides an efficient approximation that yields accurate predictions for continuous and bichromatic GB diffusivity constitutive models across a wide range of property contrast ratios (10^0 to 10^7). The efficiency of this 1-term approximation is expected to enable the consideration of GBNs within microstructure design strategies, which can require numerous function evaluations during optimization and thus require computationally efficient homogenization models. To the best of our knowledge, this is the first structure-property relation for GBNs that (a) can handle a continuous constitutive model for individual GB properties as a function of their macroscopic crystallographic parameters across the entire range of possible effective properties (i.e. sub-critical, critical, and super-critical regimes) and (b) automatically accounts for microstructural correlations that exist in real GBNs.

Application of this SGT structure-property model to a large and diverse set of microstructures elucidated the important role of GBs with intermediate properties on the effective diffusivity of GBNs even for systems with very large property contrast. This may have implications for future GBN modeling efforts.

The eigenvector corresponding to the dominant term in Eq. 4 represents a function on the domain

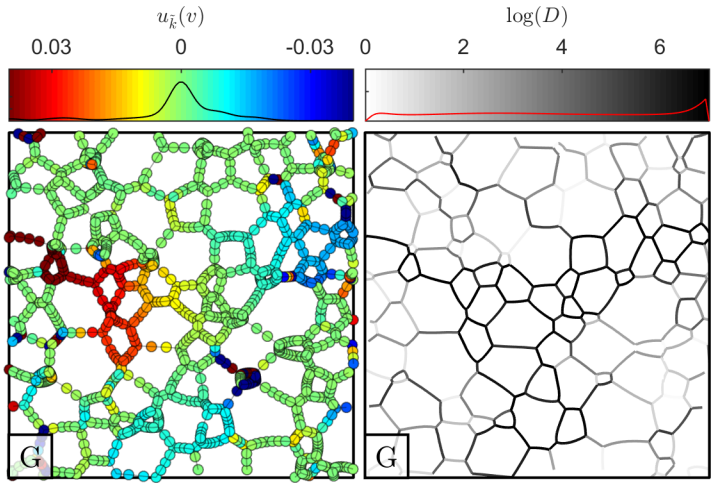

Figure 14: For the microstructure with the largest value of $\tilde{k}'$, a plot of $u_{\tilde{k}'}(v)$ is shown (in color), as well as the GBN with GB shaded by $\log(D)$ (in grayscale). The distributions $\rho[u_{\tilde{k}'}(v)]$ and $\rho[\log(D)]$ are shown in the respective colorbars, with the scale of the vertical axes identical to those from Fig. 9 to facilitate direct comparison.

of the GBN nodes, $u_{\tilde{k}}(v)$, that describes the dominant eigenmode of the GBN. Visualization of $u_{\tilde{k}}(v)$ naturally highlights the dominant features of the GBN that contribute to its aggregate behavior (i.e. D_{eff}).

In the context of continuous constitutive models, a GBN structural transition was identified, which is characterized by a fundamental change in the distribution, $\rho[u_{\tilde{k}'}(v)]$, and can be identified by means of the spectral index of the dominant term in Eq. 4, $\tilde{k}$ (or $\tilde{k}'$). Below a critical index, GBNs tend to be more homogeneous, weakly connected, and have low effective diffusivities; above this critical index GBNs become more heterogeneous, strongly connected and generally exhibit much higher effective diffusivities. Combination of the dominant spectral index and the length-weighted median of the diffusivity distribution facilitates the characterization of the structure and effective properties of GBNs with realistic continuous distributions of GB properties.

It was found that while local constraints, such as those captured by TJ fractions, do not fully specify global network connectivity, they do limit the possible global network configurations as evidenced by the bounds observed in $\tilde{k}'$ as a function of the J_i.

While these methods were developed in the context of diffusivity, the extension to other GB properties is natural and can be accomplished by replacing the weights in the GBN Laplacian with an appropriate weight related to the property of interest.

6 Acknowledgments

This material is based upon work supported by the National Science Foundation under NSF CAREER Award DMR #1654700. OKJ is grateful for conversations with Christopher A. Schuh and Jeremy K. Mason that inspired the effort to apply SGT to GBNs.

References

[1] L Tan, K Sridharan, Todd Allen, R.K. Nanstad, and D.A. McClintock. Microstructure tailoring for property improvements by grain boundary engineering. *Journal of Nuclear Materials*, 374(1-2):270–280, feb 2008.

[2] S. Bechtle, Mukul Kumar, B.P. Somerday, M.E. Launey, and R.O. Ritchie. Grain-boundary engineering markedly reduces susceptibility to intergranular hydrogen embrittlement in metallic materials. *Acta Materialia*, 57(14):4148–4157, aug 2009.

[3] E M Lehockey, D Limoges, G Palumbo, J Sklarchuk, K Tomantschger, and A Vincze. On improving the corrosion and growth resistance of positive Pb-acid battery grids by grain boundary engineering. *Journal of Power Sources*, 78(1-2):79–83, mar 1999.

[4] G Palumbo, E M Lehockey, P Lin, U Erb, and K T Aust. A Grain Boundary Engineering Approach to Materials Reliability. *MRS Proceedings*, 458:273, feb 1997.

[5] G Palumbo, P J King, K.T. Aust, U. Erb, and P.C. Lichtenberger. Grain boundary design and control for intergranular stress-corrosion resistance. *Scripta Metallurgica et Materialia*, 25(8):1775–1780, aug 1991.

[6] Wayne E King and Adam J Schwartz. Toward Optimization of the Grain Boundary Character Distribution in Copper by Strain Annealing. *MRS Proceedings*, 458(5):53, feb 1996.

[7] Visit Thaveeprungsriporn and Gary S. Was. The role of coincidence-site-lattice boundaries in creep of Ni-16Cr-9Fe at 360 C. *Metallurgical and Materials Transactions A*, 28(10):2101–2112, oct 1997.

[8] Chen Li, Yelong Wu, Jonathan D. Poplawsky, Timothy J. Pennycook, Naba Paudel, Wanjian Yin, Sarah J. Haigh, Mark P. Oxley, Andrew R. Lupini, Mowafak Al-Jassim, Stephen J. Pennycook, and Yanfa Yan. Grain-Boundary-Enhanced Carrier Collection in CdTe Solar Cells. *Physical Review Letters*, 112(15):156103, apr 2014.

[9] Jonathan D. Poplawsky, Naba R. Paudel, Chen Li, Chad M. Parish, Donovan Leonard, Yanfa Yan, and Stephen J. Pennycook. Direct Imaging of Cl- and Cu-Induced Short-Circuit Efficiency Changes in CdTe Solar Cells. *Advanced Energy Materials*, 4(15):1400454, oct 2014.

[10] D. P. Norton, A. Goyal, J. D. Budai, D. K. Christen, D. M. Kroeger, E. D. Specht, Q. He, B. Saffian, M. Paranthaman, C. E. Klabunde, D. F. Lee, B. C. Sales, and F. A. List. Epitaxial YBa2Cu3O7 on Biaxially Textured Nickel (001): An Approach to Superconducting Tapes with High Critical Current Density. *Science*, 274(5288):755–757, nov 1996.

[11] D.R. Olander. Fundamental aspects of nuclear reactor fuel elements. Technical report, Technical Information Center, U.S. Department of Energy, jan 1976.

[12] HC Lim, K Rudman, K Krishnan, Robert McDonald, Patricia Dickerson, Darrin Byler, Pedro Peralta, Chris Stanek, and Kenneth McClellan. Microstructurally Explicit Simulation of Intergranular Mass Transport in Oxide Nuclear Fuels. *Nuclear Technology*, 182(2):155–163, 2013.

[13] Paul C Millett. Percolation on grain boundary networks: Application to fission gas release in nuclear fuels. *Computational Materials Science*, 53(1):31–36, feb 2012.

[14] Jie Deng, Dane Morgan, and Izabela Szlufarska. Kinetic Monte Carlo simulation of the effective diffusivity in grain boundary networks. *Computational Materials Science*, 93:36–45, oct 2014.

[15] M. M. Moghadam, J M Rickman, M. P. Harmer, and H. M. Chan. The role of boundary variability in polycrystalline grain-boundary diffusion. *Journal of Applied Physics*, 117(4):045311, jan 2015.

[16] M.M. Moghadam, J M Rickman, M.P. Harmer, and H.M. Chan. Orientational anisotropy and interfacial transport in polycrystals. *Surface Science*, 646:204–209, apr 2016.

[17] Srikanth Patala, Jeremy K Mason, and Christopher A Schuh. Improved representations of misorientation information for grain boundary science and engineering. *Progress in Materials Science*, 57(8):1383–1425, nov 2012.

[18] Megan E Frary and Christopher A Schuh. Grain boundary networks: Scaling laws, preferred cluster structure, and their implications for grain boundary engineering. *Acta Materialia*, 53(16):4323–4335, sep 2005.

[19] Thomas Wanner, Edwin R. Fuller Jr., and David M Saylor. Homology metrics for microstructure response fields in polycrystals. *Acta Materialia*, 58(1):102–110, jan 2010.

[20] Gregory S Rohrer and Herbert M. Miller. Topological characteristics of plane sections of polycrystals. *Acta Materialia*, 58(10):3805–3814, jun 2010.

[21] V Y Gertsman and K. Tangri. Computer simulation study of grain boundary and triple junction distributions in microstructures formed by multiple twinning. *Acta Metallurgica et Materialia*, 43(6):2317–2324, jun 1995.

[22] Christopher A Schuh, Mukul Kumar, and Wayne E King. Universal features of grain boundary networks in FCC materials. *Journal of Materials Science*, 40(4):847–852, feb 2005.

[23] Mukul Kumar, Wayne E King, and Adam J Schwartz. Modifications to the microstructural topology in f.c.c. materials through thermomechanical processing. *Acta Materialia*, 48(9):2081–2091, may 2000.

[24] P Fortier, K Aust, and W Miller. Effects of symmetry, texture and topology on triple junction character distribution in polycrystalline materials. *Acta Metallurgica et Materialia*, 43(1):339–349, jan 1995.

[25] Megan E Frary and Christopher A Schuh. Percolation and statistical properties of low- and high-angle interface networks in polycrystalline ensembles. *Physical Review B*, 69(13):134115, apr 2004.

[26] Megan E Frary and Christopher A Schuh. Connectivity and percolation behaviour of grain boundary networks in three dimensions. *Philosophical Magazine*, 85(11):1123–1143, apr 2005.

[27] Jeremy K Mason, Emanuel A. Lazar, Robert D MacPherson, and David J Srolovitz. Statistical topology of cellular networks in two and three dimensions. *Physical Review E*, 86(5):051128, nov 2012.

[28] Jeremy K Mason, Oliver K Johnson, Bryan Walter Reed, Shiu Fai Li, James S. Stolken, and Mukul Kumar. Statistics of twin-related domains and the grain boundary network. *Acta Materialia*, 61(17):6524–6532, oct 2013.

[29] Bryan Walter Reed, Mukul Kumar, Roger W Minich, and Robert E Rudd. Fracture roughness scaling and its correlation with grain boundary network structure. *Acta Materialia*, 56(13):3278–3289, aug 2008.

[30] Sergey Brin and Lawrence Page. The anatomy of a large-scale hypertextual Web search engine. *Computer Networks and ISDN Systems*, 30(1-7):107–117, apr 1998.

[31] Oliver Bastert, Dan Rockmore, Peter F. Stadler, and Gottfried Tinhofer. Landscapes on spaces of trees. *Applied Mathematics and Computation*, 131(2-3):439–459, sep 2002.

[32] Georgios A Pavlopoulos, Maria Secrier, Charalampos N Moschopoulos, Theodoros G Soldatos, Sophia Kossida, Jan Aerts, Reinhard Schneider, and Pantelis G Bagos. Using graph theory to analyze biological networks. *BioData Mining*, 4(1):10, dec 2011.

[33] Phillip P A Staniczenko, Jason C Kopp, and Stefano Allesina. The ghost of nestedness in ecological networks. *Nature Communications*, 4:1391, jan 2013.

[34] M E J Newman. *Networks: An Introduction*. OUP Oxford, 2010.

[35] Lawrence Page, Sergey Brin, Rajeev Motwani, and Terry Winograd. The PageRank Citation Ranking: Bringing Order to the Web. Technical Report 1999-66, Stanford InfoLab, nov 1999.

[36] Mark Kac. Can One Hear the Shape of a Drum? *The American Mathematical Monthly*, 73(4):1, apr 1966.

[37] Wendy Ellens. *Effective resistance and other graph measures for network robustness*. Ms, Leiden University, 2011.

[38] Wendy Ellens, F.M. Spieksma, P. Van Mieghem, A. Jamakovic, and R.E. Kooij. Effective graph resistance. *Linear Algebra and its Applications*, 435(10):2491–2506, nov 2011.

[39] Lennard Kamenski, Weizhang Huang, and Hongguo Xu. Conditioning of finite element equations with arbitrary anisotropic meshes. *Mathematics of Computation*, 83(289):2187–2211, mar 2014.

[40] Ramaseshan Kannan, Stephen Hendry, Nicholas J. Higham, and Françoise Tisseur. Detecting the causes of ill-conditioning in structural finite element models. *Computers & Structures*, 133:79–89, mar 2014.

[41] I. Fried. Bounds on the extremal eigenvalues of the finite element stiffness and mass matrices and their spectral condition number. *Journal of Sound and Vibration*, 22(4):407–418, jun 1972.

[42] Emanuel A. Lazar, Robert D MacPherson, and David J Srolovitz. A more accurate two-dimensional grain growth algorithm. *Acta Materialia*, 58(2):364–372, jan 2010.

[43] Christopher A Schuh and Megan E Frary. Correlations beyond the nearest-neighbor level in grain boundary networks. *Scripta Materialia*, 54(6):1023–1028, mar 2006.

[44] Ying Chen and Christopher A Schuh. Coble creep in heterogeneous materials: The role of grain boundary engineering. *Physical Review B*, 76(6):1–13, aug 2007.

[45] Ying Chen and Christopher a Schuh. Diffusion on grain boundary networks: Percolation theory and effective medium approximations. *Acta Materialia*, 54(18):4709–4720, oct 2006.

[46] C. Yeong and Salvatore Torquato. Reconstructing random media. *Physical Review E*, 57(1):495–506, jan 1998.

[47] Megan E Frary and Christopher A Schuh. Correlation-space description of the percolation transition in composite microstructures. *Physical Review E*, 76(4):42–45, oct 2007.

[48] Lin Li and Sharniece Holland. Grain boundary diffusion: non-random topology and effective medium approximation. *Nanomaterials and Energy*, 3(4):139–147, jul 2014.

[49] W. S. Tong, J M Rickman, H. M. Chan, and M. P. Harmer. Coble-creep response and variability of grain-boundary properties. *Journal of Materials Research*, 17(02):348–352, feb 2002.

[50] D Moldovan, D. Wolf, S. R. Phillpot, A. K. Mukherjee, and H. Gleiter. Grain-boundary diffusion-controlled stress concentration in polycrystals. *Philosophical Magazine Letters*, 83(1):29–38, jan 2003.

[51] Oliver K Johnson and Christopher A Schuh. Texture mediated grain boundary network design in two dimensions. *Journal of Materials Research*, 31(09):1171–1184, may 2016.

[52] Oliver K Johnson, Lin Li, Michael J Demkowicz, and Christopher A Schuh. Inferring grain boundary structureproperty relations from effective property measurements. *Journal of Materials Science*, 50(21):6907–6919, nov 2015.

[53] M Biscondi. Intergranular diffusion and grain-boundary structure. In P Lacombe, editor, *Physical Chemistry of the Solid State: Applications to Metals and their Compounds*, pages 225–239, Amsterdam, 1984. Elsevier Science Publishers B.V.

[54] J Sommer, Chr Herzig, S Mayer, and Wolfgang Gust. Grain Boundary Self-Diffusion in Silver Bicrystals. *Defect and Diffusion Forum*, 66-69:843–848, 1989.

[55] Brent L Adams, Surya R Kalidindi, and David T Fullwood. Higher-Order Microstructure Representation 12. In *Microstructure-Sensitive Design for Performance Optimization*, pages 249–268. Butterworth-Heinemann, Waltham, 1 edition, 2012.

[56] Richard Zallen. Polychromatic percolation: Coexistence of percolating species in highly connected lattices. *Physical Review B*, 16(4):1426–1435, aug 1977.

[57] F Y Wu and H E Stanley. Polychromatic Potts model: a new lattice-statistical problem and some exact results. *Journal of Physics A: Mathematical and General*, 16(18):L751–L755, dec 1983.

[58] Massimiliano Giona and Alessandra Adrover. Multicomponent percolation: Probabilistic properties and application to nonisothermal reactions in granular materials. *Physical Review E*, 49(6):5287–5294, jun 1994.

[59] J. W. Halley and W. K. Holcomb. Conductivity of a Three-Component "Reactive" Percolation Model. *Physical Review Letters*, 40(25):1670–1673, jun 1978.

[60] A Coniglio and F Peruggi. Clusters and droplets in the q-state Potts model. *Journal of Physics A: Mathematical and General*, 15(6):1873–1883, jun 1982.

[61] Huaijun Qiu and Edwin R. Hancock. Graph matching and clustering using spectral partitions. *Pattern Recognition*, 39(1):22–34, jan 2006.

[62] M E J Newman. Modularity and community structure in networks. *Proceedings of the National Academy of Sciences*, 103(23):8577–8582, jun 2006.

[63] Andy D Perkins and Michael A Langston. Threshold selection in gene co-expression networks using spectral graph theory techniques. *BMC Bioinformatics*, 10(Suppl 11):S4, jan 2009.

[64] D.A. Tolliver and G.L. Miller. Graph Partitioning by Spectral Rounding: Applications in Image Segmentation and Clustering. In *2006 IEEE Computer Society Conference on Computer Vision and Pattern Recognition - Volume 1 (CVPR'06)*, volume 1, pages 1053–1060. IEEE, 2006.

[65] Alberto Paccanaro. Spectral clustering of protein sequences. *Nucleic Acids Research*, 34(5):1571–1580, mar 2006.

[66] J. Malik. Normalized cuts and image segmentation. *IEEE Transactions on Pattern Analysis and Machine Intelligence*, 22(8):888–905, 2000.

[67] Christopher A Schuh, Mukul Kumar, and Wayne E King. Analysis of grain boundary networks and their evolution during grain boundary engineering. *Acta Materialia*, 51(3):687–700, feb 2003.

[68] Brendan J. Frey and Delbert Dueck. Clustering by Passing Messages Between Data Points. *Science*, 315(5814):972–976, feb 2007.

[69] J. Lin. Divergence measures based on the Shannon entropy. *IEEE Transactions on Information Theory*, 37(1):145–151, 1991.

[70] Vasily V Bulatov, Bryan Walter Reed, and Mukul Kumar. Grain boundary energy function for fcc metals. *Acta Materialia*, 65:161–175, feb 2014.

[71] W Bollmann. Triple lines in polycrystalline aggregates as disclinations. *Philosophical Magazine A*, 49(1):73–79, jul 1984.

[72] Vinay Ambegaokar, B. Halperin, and J. Langer. Hopping Conductivity in Disordered Systems. *Physical Review B*, 4(8):2612–2620, 1971.